Editors' Suggestion | Featured in Physics

Hydrodynamics of the Viscous Electron Fluid in Cadmium

Xiaodong Guo,[1,2] Xiaokang Li,[1] Benoît Fauqué,[2] Alaska Subedi,[3] Lingxiao Zhao,[4,5,*] Zengwei Zhu,[1,†] and Kamran Behnia[2,‡]

[1]*Wuhan National High Magnetic Field Center and School of Physics, Huazhong University of Science and Technology, Wuhan 430074, China*

[2]*Laboratoire de Physique et d'Étude de Matériaux (CNRS) ESPCI Paris, PSL Research University, 75005 Paris, France*

[3]*CPHT, CNRS, École polytechnique, Institut Polytechnique de Paris, 91120 Palaiseau, France*

[4]*Quantum Science Center of Guangdong-HongKong-Macao Greater Bay Area, Shenzhen 523335, China*

[5]*Department of Physics, Southern University of Science and Technology, Shenzhen, China*

(Received 24 April 2026; accepted 19 August 2026; published 9 November 2026)

Thanks to electron-electron (*e*-*e*) collisions conserving momentum, metallic electron fluids are viscous. Yet, this viscosity is rarely detectable in bulk transport. Here, we report on the canonical realization of the Gurzhi effect in an elemental three-dimensional metal: cadmium. Using focused ion beam microstructuring to tune the effective thickness, we detected a low-temperature size-dependent resistivity upturn in a finite window sandwiched between ballistic and diffusive regimes. Within this window, the electrical conductivity displays a simultaneous quadratic dependence on both sample size and temperature—fingerprint of a hydrodynamic flow. This leads us to quantify the amplitude and the temperature dependence of kinematic and dynamic viscosity of the electron fluid. In cadmium, in contrast with graphene and ^{3}He, the rate of momentum-conserving *e*-*e* collisions is not set by the main Fermi energy, but by Lilliputian energy scales and intervalley bottlenecks.

DOI: 10.1103/g32f-j6q2

According to empirical knowledge, accessible in a kitchen, warming a liquid reduces its viscosity. This is also true for quantum liquids such as normal ^{3}He at cryogenic temperatures: warming enhances fermion-fermion collisions rate, diminishing viscosity [1]. In apparent contrast, the electrical conductivity of a metallic electronic liquid worsens by warming. The fundamental reason for this difference is that most collisions suffered by electrons, instead of conserving their momentum, relax it. Their multiplication enhances resistivity and not conductivity.

However, hydrodynamic corrections to electronic transport are expected to emerge whenever the quasiparticle momentum is approximately conserved [2–4]. Decades ago, Gurzhi [5,6] assumed a metallic system where the momentum-conserving (MC) mean free path, ℓ_{mc}, becomes shorter than both the sample size and the momentum-relaxing (MR) mean free path, ℓ_{mr}. In this case, the momentum and energy of the traveling electrons are no longer lost to the outside bath. The flow becomes viscous, and warming would reduce the electric resistivity of the metal [2].

This appealing picture is hard to realize experimentally. For ℓ_{mc} to become the shortest length scale, the temperature should be sufficiently low (to make collision by phonons negligible) yet finite (to have sufficiently frequent collisions between electrons). The phase space for *e*-*e* collisions follows $(T/T_F)^2$. Most of these collisions, presumably because they are Umklapp events, do not conserve momentum. The experimental fingerprint of *e*-*e* collisions has been a T-square enhancement of electrical resistivity (and not conductivity) [7].

In the past few years, experiments have documented a hydrodynamic regime sandwiched between diffusive and ballistic regimes in several metals. Imaging techniques have found that in this regime, the electron drift velocity is attenuated at the boundaries, due to the viscosity-induced shear forces at the channel walls, a phenomenon dubbed Poiseuille flow in the classical fluid mechanics [8–11]. Corrections to transport properties due to hydrodynamics have also been reported [12–16] notably in thermal transport [17–19]. With the exception of 2D graphene [2,14,20], however, a clear bulk hydrodynamic behavior, in which *e*-*e* collisions enhance conduction (instead of resistance) has remained elusive.

In this context, focused ion beam (FIB) etching technology [21,22] has emerged as an efficient tool for shrinking without introducing additional defects. By reducing the sample width while keeping ℓ_{mr} under control, one can fine-tune the width of the hydrodynamic window sandwiched between the diffusive and ballistic transport regimes [12,18].

*Contact author: zhaolingxiao@quantumsc.cn

†Contact author: zengwei.zhu@hust.edu.cn

‡Contact author: kamran.behnia@espci.fr

 © 2026 American Physical Society

Here, we report on the observation of hydrodynamic electron flow that constitutes the canonical realization of the Gurzhi effect in micron-sized cadmium samples, tailored by FIB from high purity single crystals with a residual resistivity of $\rho_0 \sim 3$ nΩ cm and a residual resistivity ratio [RRR $= \rho(300\ \mathrm{K})/\rho_0$] of ∼3000. We find that as the effective thickness shrinks from 114 μm to 12 μm, transport at cryogenic temperatures evolves from diffusive to hydrodynamic. A canonical hydrodynamic behavior, in which conductivity scales with the square of temperature and the square of the size, is observed for the first time in an elemental three-dimensional metal. As expected, the hydrodynamic regime is restricted to a finite window of temperature and thickness. At very low temperatures and in very thin samples, a ballistic regime is recovered. We quantify the dynamic and kinematic viscosity of this electron liquid and compare it to those of classical and quantum fluids. The rate of momentum-conserving *e*-*e* collisions in cadmium is orders of magnitude smaller than the momentum-relaxing ones, which is set by the large Fermi energy of the main pockets. Our *ab initio* DFT calculations of the electronic band structure identify narrow bottlenecks between pockets and valleys of the Fermi surface with low energy scales allowing frequent momentum exchange in small fermion reservoirs and across valleys and pockets.

Hexagonal close-packed (HCP) cadmium is a compensated metal [22,23]. Its Fermi surface [Fig. 1(a)] consists of an electron pocket (the "lens") and two hole pockets (the "cap" and the "monster"). We tailored samples of mesoscopic dimensions with electrodes to measure their resistivity [Fig. 1(b)]. The evolution of the electrical resistivity with temperature and size is shown in Fig. 1(c). At room temperature, $\rho(273\ \mathrm{K}) \simeq 6.5$ μΩ cm, consistent with what has been reported in bulk cadmium [24]. This consistency continues down to 20 K, and below this temperature a size dependence emerges. The largest sample had an effective cross-sectional area of $s = 114$ μm ($s = \sqrt{w \times t}$, w is the width and t the thickness) displays the metallic behavior of bulk cadmium. Those with $s \leq 64.8$ μm display a non-monotonic resistivity, steadily amplified with decreasing s [see Supplemental Material (SM) Note 1 [25] for sample dimension details]. In the thinnest sample ($s = 12$ μm), at $T = 2$ K, resistivity becomes 1.4 larger than its minimum value at 4.6 K. Absent Anderson localization or Kondo impurities, the observed resistivity upturn can be safely identified as the one expected when the electron fluid flows viscously. It is reminiscent of graphene constrictions, in which for a width of 0.5 μm and a density of $n = 0.5 \times 10^{12}$ cm^{-2} resistivity at 2 K rises to a value ∼1.2 times its minimum value at 150 K [2,14,20].

The standard description of electrical transport in elemental metals is built on Bloch-Grüneisen (BG) picture [35]. Electron-phonon scattering leads to $\rho \propto T$ at high temperatures and to $\rho \propto T^5$ at low temperatures (when the typical phonon wave vector is much smaller than the Fermi radius). The relevance of this picture can be checked by

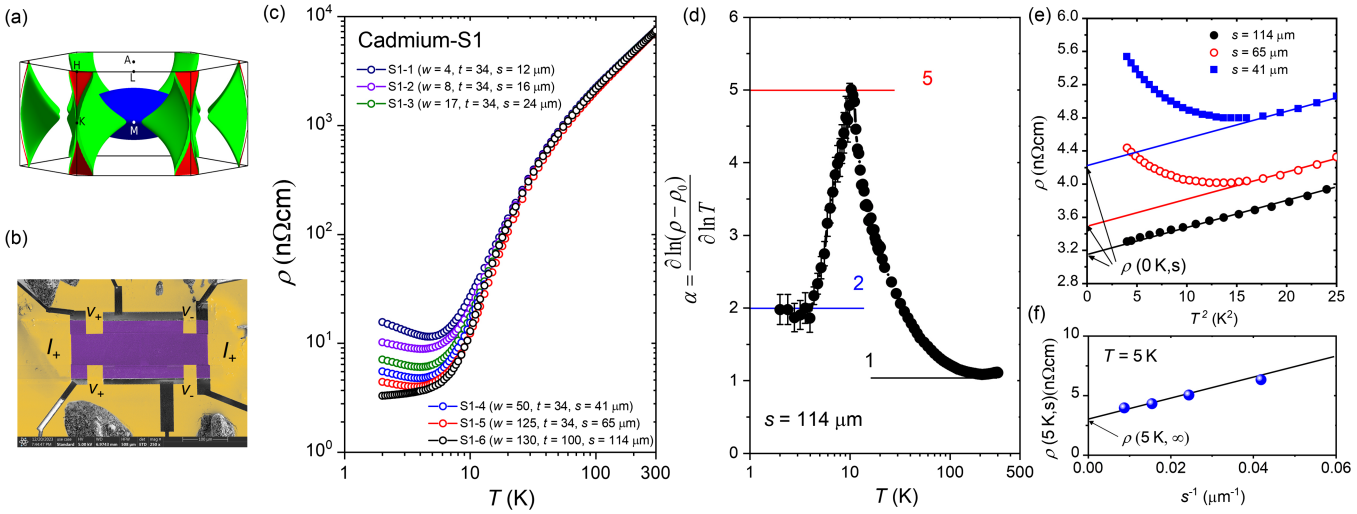


FIG. 1. Size dependence of electrical resistivity. (a) Fermi surface of HCP Cd consisting of hole-type "cap" (red), hole-type "monster" (green), and electron-type "lens" (blue) sheets. (b) False color image of Cd microstructures (purple) and electrodes (yellow) obtained with a scanning electron microscope. In this lamella, the sample plane is perpendicular to the [0001] direction, and the current is applied along the $[\bar{1}2\bar{1}0]$ direction. (c) Evolution of the temperature dependence of electrical resistivity of a cadmium crystal as the effective thickness ($s = \sqrt{w \times t}$) is reduced. The latter is the geometric average of width (w) and thickness (t). Below 5 K, an upturn emerges. Note that in samples S1-1 to S1-5, the thickness was kept constant while the width was progressively reduced. (d) The exponent of the inelastic resistivity ($\rho = \rho_0 + AT^\alpha$), determined from the logarithmic derivative of $(\rho - \rho_0)$ in sample $s = 114$ μm as a function of temperature. (e) Resistivity as a function of the square of temperature. The slope of the linear fit ($A \simeq 0.03 \pm 0.002$ nΩ cm K^{-2}) does not change with s but the intercept increases with decreasing s. (f) 5 K resistivity as a function of the inverse of s. As expected in the ballistic picture, the dependence is linear with a slope of $a \simeq 8.8 \pm 0.3 \times 10^{-16}\ \Omega \cdot \mathrm{m}^2$.

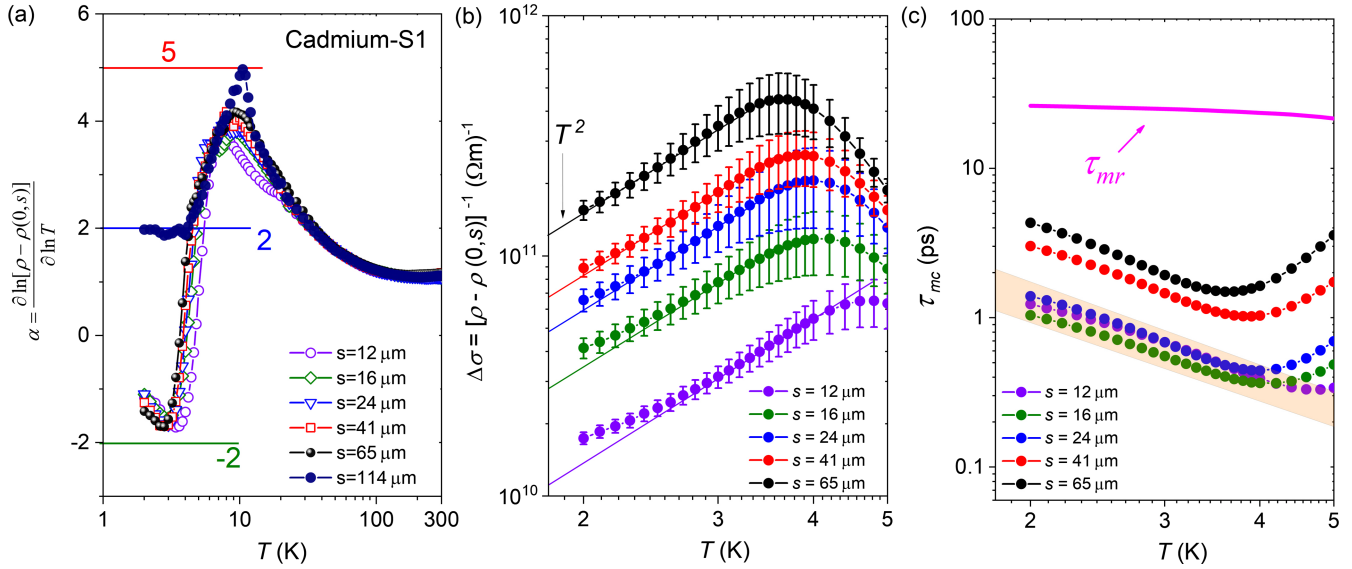


FIG. 2. Extracting the hydrodynamic contribution to electrical conductance. (a) Exponent of the temperature dependence of the electrical resistivity, α as function of the temperature determined by taking the logarithmic derivative after subtracting $\rho(0,s) = \rho(0,\infty) + as^{-1}$. Below 5 K, α approaches–2, indicating the emergence of a conductivity quadratic in temperature. (b) Temperature dependence of $\Delta\sigma = 1/[\rho - \rho(0,s)]$. At low temperature, $\Delta\sigma \propto T^2$. (c) Momentum-conserving scattering time, τ_{mc}, extracted from $\Delta\sigma$ and Eq. (1) in different samples. Also shown is the momentum-relaxing scattering time, τ_{mr}. In all samples, the hydrodynamic hierarchy holds: $\tau_{mc} \ll \tau_{mr}$. The three thinnest samples have a virtually identical τ_{mc}.

expressing resistivity as $\rho = \rho_0 + AT^\alpha$ and extracting α from the experimental data. Taking a logarithmic derivative leads us to $\alpha = \{[\partial \ln(\rho - \rho_0)]/(\partial \ln T)\}$. The result of this analysis for the thickest sample ($s = 114$ μm) is shown in Fig. 1(d). As previously noticed for other semimetals [36], with cooling α steadily increases, passing from room temperature $\simeq$1 to 10 K $\simeq$ 5. Below this temperature, α suddenly drops and becomes $\simeq$2 below 2 K. This purely quadratic temperature dependence corresponds to a regime in which the only channel of inelastic scattering is resistive collisions with other electrons [36].

Figure 1(e) plots the low temperature resistivity as a function of T^2 in the three thickest samples. The diffusive picture of charge transport is disrupted by electron hydrodynamics below a threshold sample size. In the thicker sample ($s = 114$ μm), resistivity is the sum of constant ($\rho_0 = 3.25$ nΩ · cm) and quadratic (AT^2) terms. The prefactor of the latter ($A = 0.03$ nΩ · cm · K^{-2}) fills in the trend seen across elemental semimetals [37] (see SM Note 2 [25]). In thinner samples, a low-temperature upturn emerges on top of this T-quadratic resistivity. Figure 1(e) shows that shrinking s modifies the intercept (ρ_0), but not the slope (A). To quantify α in samples with resistivity upturn, the rigid upward shift of finite-temperature resistivity induced by thinning is to be taken into account.

Figure 1(f) is a plot of 5 K resistivity as a function of the inverse of the effective thickness. One can see that $\rho(5\text{ K}, s)$ increases linearly with s^{-1}, as expected in the diffusive-ballistic picture. The 5 K resistivity of a sample with effective thickness of s is equal to $\rho(5\text{ K}, s) = \rho(5\text{ K}, \infty) + as^{-1}$. The slope of this linear enhancement ($a \simeq 9 \times 10^{-16}$ Ω · m^2) corresponds to the upper limit of ballistic transport in quantitative agreement with the Fuchs-Sondheimer picture of ballistic transport [38] and with a previous report [39] (see SM Note 3 [25]). The intercept of the linear fit in Fig. 1(d) [$\rho(5\text{ K}, \infty) = 3$ nΩ·cm] represents 5 K resistivity in an infinite sample with a disorder level equal to samples of finite size. Since varying thickness does not affect A, the zero-temperature resistivity of an infinite sample is $\rho(0\text{ K}, \infty) = \rho(5\text{ K}, \infty) - 5^2A = 2.3 \pm 0.05$ nΩ·cm. This is the residual resistivity due to scattering by defects (and not the boundary).

Expressing now resistivity as $\rho(T, s) = \rho(0, s) + AT^\alpha$, where $\rho(0, s) = \rho(0, \infty) + as^{-1}$, the logarithmic derivative yields $\alpha = \{\partial \ln[\rho - \rho(0, s)]\}/(\partial \ln T)$. The result is shown in Fig. 2(a). One can see that the upturn in resistivity for $s \leq 64.8$ μm, leads to $\alpha \sim -2$ between 2 and 5 K. The temperature and size dependence of the intrinsic electrical conductivity after subtraction of the size-dependent residual resistivity, $\Delta\sigma(T, s) = [\rho - \rho(0, s)]^{-1}$, is shown in Fig. 2(b). Below $T = 5$ K, $\Delta\sigma \propto T^2$. This T-square dependence is the canonical hydrodynamic behavior. A deviation from this behavior, visible at low temperature ($T < 2.5$ K) and small thickness ($s < 20$ μm) is a precursor of the ballistic regime. As discussed below, the hydrodynamic regime vanishes when the momentum conserving mean free path exceeds the sample thickness.

The hydrodynamic contribution to the electrical conductivity scales with the momentum-conserving collision time, τ_{mc}, following [15,40]

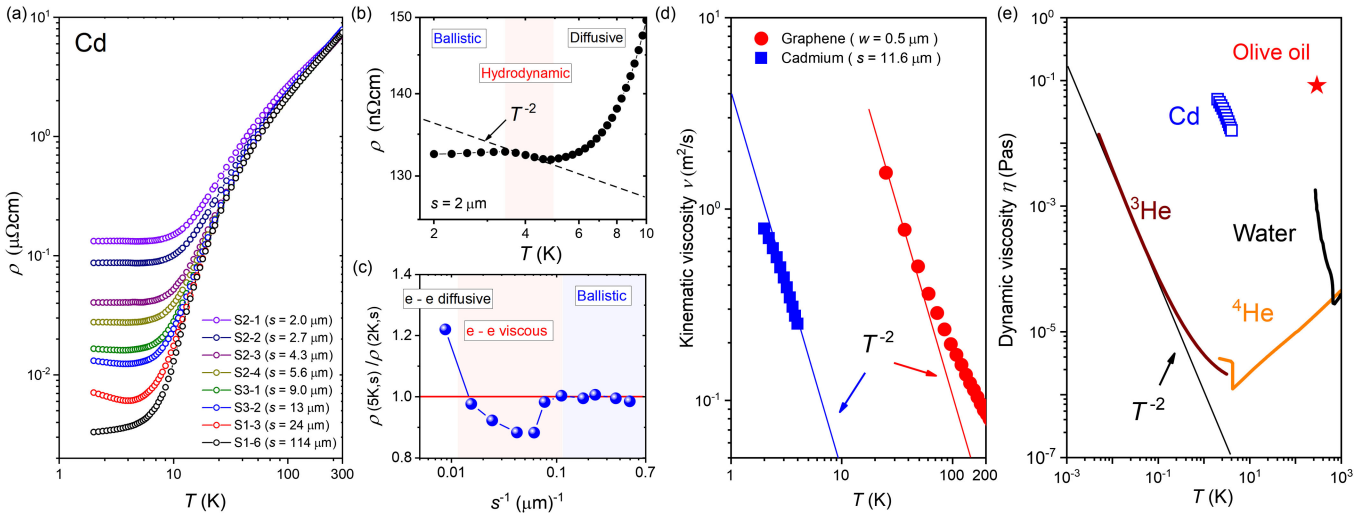


FIG. 3. Hydrodynamic to ballistic transition and viscosity comparison. (a) Variation of resistivity with decreasing s from 114 μm to 2 μm. The mechanism turns from diffusive to hydrodynamic and then to ballistic. (b) The temperature dependence of resistivity for $s = 2$ μm sample. Resistivity increases from 5 to 3.5 K, and then remains constant, indicating a transition from hydrodynamic to ballistic transport. (c) The ratio of $[\rho(5\ \mathrm{K}, s)]/[\rho(2\ \mathrm{K}, s)]$ as a function of s^{-1}. (d) Kinematic viscosity as function of temperature in Cd and in graphene [2,14]. In both cases, there is an asymptotic T^{-2} behavior in the low temperature limit. (e) Comparison of the dynamic viscosity, η, of the electron fluid in cadmium with ^{3}He [42], ^{4}He [43], water, and olive oil [44].

$$\Delta\sigma = \frac{1}{3}\frac{ne^2}{m^*}\frac{s^2}{v_F^2\tau_{mc}}. \tag{1}$$

This expression is reminiscent of the Drude conductivity, with scattering time replaced by a time scale of $(s^2)/(v_F^2\tau_{mc})$ and with $\ell_{mc} = \tau_{mc}v_F$. Figure 2(c) is a plot of τ_{mc} for five samples derived from the experimental data and Eq. (1) using $v_F = 1600$ km/s and $n = 3.48 \times 10^{22}$ cm^{-3}. Note that this is a single-band isotropic treatment with obvious limits, which are discussed in SM Note 3 [25]. Also shown is τ_{mr} extracted from the temperature dependence of resistivity in the thickest sample.

As the thickness is decreased further, the hydrodynamic window closes. Data obtained on samples thinned below 10 μm are shown in Fig. 3(a). The hydrodynamic upturn resistivity is gradually suppressed with decreasing s. When $s < 5.6$ μm and $T < 3.5$ K, $\rho \propto T^0$: the resistivity becomes temperature-independent, uniquely depending on s [25], indicating a transition from the hydrodynamic to the ballistic regime. This is consistent with Gurzhi's picture [5,6,41]. The temperature dependence of the resistivity of the $s = 2$ μm sample is shown in Fig. 3(b). A modest resistivity upturn below 5 K abruptly stops at ∼4 K. At lower temperatures, resistivity becomes flat, with the extracted mean free path of the order of thickness. Figure 3(c) shows the ratio of $[\rho(5\ \mathrm{K}, s)]/[\rho(2\ \mathrm{K}, s)]$ as a function of s^{-1}. It becomes less than 1 in the hydrodynamic regime, sandwiched between the diffusive and ballistic regimes as the size shrinks.

The extracted kinematic viscosity ν follows a T^{-2} dependence, as in graphene [Fig. 3(d)] [14], while the corresponding dynamic viscosity η is compared with those of quantum and classical liquids in Fig. 3(e) (see End Matter Appendix A).

Table I compares three liquids of fermions (^{3}He, graphene, and Cd). Their prefactor of T-square kinematic viscosity (νT^2) differ by many orders of magnitude. The difference in the extracted $\tau_{mc}T^2$ is less drastic. Note that, in contrast to the other two cases, there are two (momentum-conserving and momentum-relaxing) time scales. The amplitude of the prefactor of T-square resistivity A in bulk Cd yields $\tau_{mr}T^2 \sim 2.4 \times 10^3$ ps · K^2, 3 orders of magnitude larger than $\tau_{mc}T^2$.

TABLE I. Comparison of three quantum fluids. The Fermi temperature, the Fermi velocity, and the prefactor of T-square viscosity in ^{3}He, graphene, and cadmium. In the latter case, there are multiple pockets, lengths, and energy scales.

System	T_F (K)	v_F (km/s)	νT^2(m^2 s^{-1} K^2))	$\tau_{mc}T^2$ (ps K^2))	Temperaturewindow (K)	Reference
^{3}He ($n = 1.63 \times 10^{22}$ cm^{-3})	2	0.057	4.2×10^{-9}	1.3	< 0.02	[45,46]
Graphene ($n = 0.5 \times 10^{12}$ cm^{-2})	1800	1000	970	3200	20–70	[2,14]
Cd ($n = p = 3.48 \times 10^{22}$ cm^{-3})	5.6–35 000	1600	3.98	6.2	2–4	[23,39]

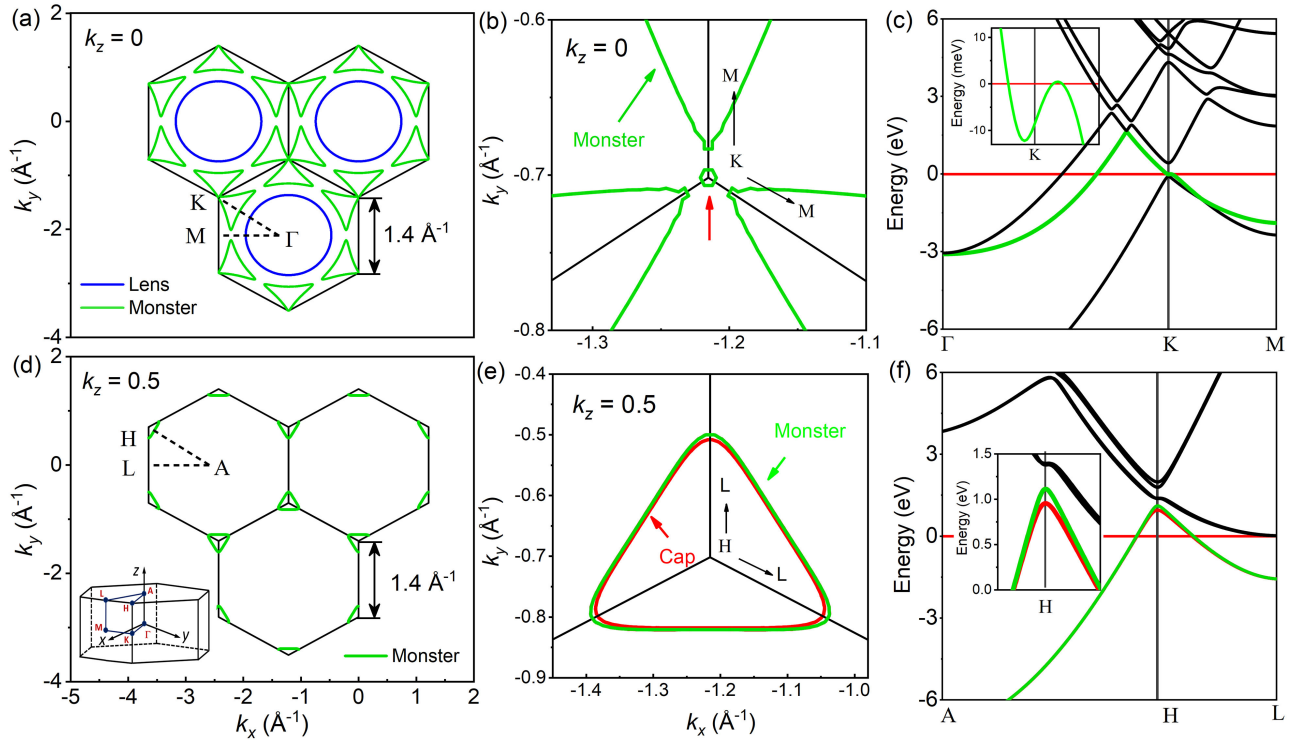


FIG. 4. Fermi surface cross section and band structure in HCP Cd. (a) Cross section of the Fermi surface at $k_z = 0$, covering three Brillouin zones. The "monster" and "lens" contours are indicated by green and blue lines. (b) Enlarged view of the "monster" hole pocket around the K point. Here, the red arrow indicates the Lilliputian Fermi surface. (c) The band structure along the $\Gamma \rightarrow$ K $\rightarrow$ M direction. (d) The contours of the "monster" are specified at $k_z = 0.5$. (e) Enlarged view at $k_z = 0.5$ shows that the "monster" and "cap" hole-type pockets are close to each other but are not degenerate. (f) The band structure along the A $\rightarrow$ H $\rightarrow$ L direction.

In a single-component isotropic Fermi liquid with $\mathcal{O}(1)$ Landau parameters, the fermion-fermion collision rate is set by the Fermi energy [1,47,48]:

$$\tau_{\text{col.}} \approx \frac{\hbar E_F}{(k_B T)^2}. \tag{2}$$

A Fermi energy of $\approx$1 eV, the order of magnitude for the large Fermi surface pockets in Cd, would give a reasonable account of its $\tau_{mr}T^2$, but the much shorter $\tau_{mc}T^2$ requires the relevance of much smaller energy scales. *Ab initio* calculations identify such Lilliputian energy scales and intervalley bottlenecks near the K point (Fig. 4) [25], consistent with low-field magnetic breakdown in Cd [49–51] (see End Matter Appendix B).

In summary, Cd crystals thinned down to micrometric dimensions display an upturn in electrical resistivity restricted to a finite window of temperature and sample size. When the ballistic linear size dependence is subtracted, one finds, on top of the diffusive contribution, a distinct conductance component that, as expected in the hydrodynamic picture of an electron fluid, scales quadratically with both size and temperature. The computed band structure reveals small and Lilliputian energy scales in addition to those associated with the main Fermi pockets. Multiplicity of energy scales and electronic reservoirs is expected to play a role in any quantitative account of our findings, a task for future studies.

Acknowledgments—We thank M. Feigel'man and A. Lucas for helpful discussions. This work was supported by the National Natural Science Foundation of China (Grants No. 12474043, No. 52588101, No. 12004123, and No. 51861135104), the Cai Yuanpei Franco-Chinese Program (No. 51258NK), the National Key Research and Development Program of China (Grant No. 2022YFA1403500), the Fundamental Research Funds for the Central Universities (Grant No. 2019kfyXMBZ071), and the Agence Nationale de la Recherche (Grant No. ANR-22-CE30-0032). X. L. was supported by the National Key Research and Development Program of China (Grant No. 2023YFA1609600) and the National Natural Science Foundation of China (Grant No. 12304065).

Data availability—The data that support the findings of this study are available from the authors upon reasonable request.

[1] E. R. Dobbs, *Helium Three* (Oxford University Press, New York, 2000).

[2] M. Polini and A. Geim, Viscous electron fluids, Phys. Today **73**, No. 6, 28 (2020).

[3] L. Fritz and T. Scaffidi, Hydrodynamic electronic transport, Annu. Rev. Condens. Matter Phys. **15**, 17 (2024).

[4] A. Hui and B. Skinner, Hydrodynamics of the electronic Fermi liquid: A pedagogical overview, J. Phys. Condens. Matter **37**, 363001 (2025).

[5] R. Gurzhi, Hydrodynamic effects in solids at low temperature, Sov. Phys. Usp. **11**, 255 (1968).

[6] R. N. Gurzhi, Minimum of resistance in impurity-free conductors, Sov. Phys. JETP **17**, 521 (1963), https://www.jetp.ras.ru/cgi-bin/e/index/e/17/2/p521?a=list..

[7] K. Behnia, On the origin and the amplitude of T-square resistivity in Fermi liquids, Ann. Phys. (Berlin) **534**, 2100588 (2022).

[8] A. Aharon-Steinberg, T. Völkl, A. Kaplan, A. K. Pariari, I. Roy, T. Holder, Y. Wolf, A. Y. Meltzer, Y. Myasoedov, M. E. Huber *et al.*, Direct observation of vortices in an electron fluid, Nature (London) **607**, 74 (2022).

[9] J. A. Sulpizio, L. Ella, A. Rozen, J. Birkbeck, D. J. Perello, D. Dutta, M. Ben-Shalom, T. Taniguchi, K. Watanabe, T. Holder *et al.*, Visualizing poiseuille flow of hydrodynamic electrons, Nature (London) **576**, 75 (2019).

[10] Z. J. Krebs, W. A. Behn, S. Li, K. J. Smith, K. Watanabe, T. Taniguchi, A. Levchenko, and V. W. Brar, Imaging the breaking of electrostatic dams in graphene for ballistic and viscous fluids, Science **379**, 671 (2023).

[11] M. L. Palm, C. Ding, W. S. Huxter, T. Taniguchi, K. Watanabe, and C. L. Degen, Observation of current whirlpools in graphene at room temperature, Science **384**, 465 (2024).

[12] P. J. W. Moll, P. Kushwaha, N. Nandi, B. Schmidt, and A. P. Mackenzie, Evidence for hydrodynamic electron flow in $PbCoO_2$, Science **351**, 1061 (2016).

[13] M. R. Van Delft, Y. Wang, C. Putzke, J. Oswald, G. Varnavides, C. A. Garcia, C. Guo, H. Schmid, V. Süss, H. Borrmann *et al.*, Sondheimer oscillations as a probe of non-ohmic flow in WP_2 crystals, Nat. Commun. **12**, 4799 (2021).

[14] R. Krishna Kumar, D. Bandurin, F. Pellegrino, Y. Cao, A. Principi, H. Guo, G. Auton, M. Ben Shalom, L. Ponomarenko, G. Falkovich *et al.*, Superballistic flow of viscous electron fluid through graphene constrictions, Nat. Phys. **13**, 1182 (2017).

[15] P. S. Alekseev, Negative magnetoresistance in viscous flow of two-dimensional electrons, Phys. Rev. Lett. **117**, 166601 (2016).

[16] A. I. Berdyugin, S. G. Xu, F. M. D. Pellegrino, R. K. Kumar, A. Principi, I. Torre, M. B. Shalom, T. Taniguchi, K. Watanabe, I. V. Grigorieva, M. Polini, A. K. Geim, and D. A. Bandurin, Measuring hall viscosity of graphene's electron fluid, Science **364**, 162 (2019).

[17] A. Principi and G. Vignale, Violation of the wiedemann-franz law in hydrodynamic electron liquids, Phys. Rev. Lett. **115**, 056603 (2015).

[18] J. Gooth, F. Menges, N. Kumar, and V. Süß, C. Shekhar, Y. Sun, U. Drechsler, R. Zierold, C. Felser, and B. Gotsmann, Thermal and electrical signatures of a hydrodynamic electron fluid in tungsten diphosphide, Nat. Commun. **9**, 4093 (2018).

[19] A. Jaoui, B. Fauque, and K. Behnia, Thermal resistivity and hydrodynamics of the degenerate electron fluid in antimony, Nat. Commun. **12**, 195 (2021).

[20] D. A. Bandurin, I. Torre, R. K. Kumar, M. B. Shalom, A. Tomadin, A. Principi, G. H. Auton, E. Khestanova, K. S. Novoselov, I. V. Grigorieva, L. A. Ponomarenko, A. K. Geim, and M. Polini, Negative local resistance caused by viscous electron backflow in graphene, Science **351**, 1055 (2016).

[21] P. J. Moll, Focused ion beam microstructuring of quantum matter, Annu. Rev. Condens. Matter Phys. **9**, 147 (2018).

[22] X. Guo, X. Li, L. Zhao, Z. Zhu, and K. Behnia, Scalable sondheimer oscillations driven by commensurability between two quantizations, Commun. Mater. **7**, 76 (2026).

[23] A. Subedi and K. Behnia, Deep-lying semi-dirac fermions in hexagonal close-packed cadmium, J. Phys. Condens. Matter **37**, 465501 (2025).

[24] L. Hall and F. E. E. Germann, *Survey of Electrical Resistivity Measurements on 8 Additional Pure Metals in the Temperature Range 0 to 273 K* (US National Bureau of Standards, Washington, D.C., 1970), Vol. 365.

[25] See Supplemental Material at http://link.aps.org/supplemental/10.1103/g32f-j6q2 for details of sample preparation and dimensions, the T^2 and T^5 resistivity prefactors, the size dependence of conductivity in the ballistic and hydrodynamic regimes, and the electronic-structure calculations, which includes Refs. [26–34].

[26] R. A. Matula, Electrical resistivity of copper, gold, palladium, and silver, J. Phys. Chem. Ref. Data **8**, 1147 (1979).

[27] P. D. Desai, T. K. Chu, H. M. James, and C. Y. Ho, Electrical resistivity of selected elements, J. Phys. Chem. Ref. Data **13**, 1069 (1984).

[28] B. J. C. van der Hoeven and P. H. Keesom, Specific heat of mercury and thallium between 0.35 and 4.2 °K, Phys. Rev. **135**, A631 (1964).

[29] D. L. Martin, Specific heat of copper, silver, and gold below 30 °K, Phys. Rev. B **8**, 5357 (1973).

[30] G. Seidel and P. H. Keesom, Specific heat of gallium and zinc in the normal and superconducting states, Phys. Rev. **112**, 1083 (1958).

[31] D. Rajdev and D. H. Whitmore, Debye temperature for cadmium derived from low-temperature specific-heat measurements, Phys. Rev. **128**, 1030 (1962).

[32] E. Ryan, J. Jackson, and Y. Lwin, Resistivity of solid mercury, Cryogenics **20**, 158 (1980).

[33] V. S. Tsoi, J. Bass, and P. Wyder, Studying conduction-electron/interface interactions using transverse electron focusing, Rev. Mod. Phys. **71**, 1641 (1999).

[34] P. Blaha, K. Schwarz, F. Tran, R. Laskowski, G. K. H. Madsen, and L. D. Marks, WIEN2k: An APW + lo program for calculating the properties of solids, J. Chem. Phys. **152**, 074101 (2020).

[35] J. Ziman, *Electrons and Phonons: The Theory of Transport Phenomena in Solids* (OUP, Oxford, 2001).

[36] A. Jaoui, A. Gourgout, G. Seyfarth, A. Subedi, T. Lorenz, B. Fauqué, and K. Behnia, Formation of an electron-phonon bifluid in bulk antimony, Phys. Rev. X **12**, 031023 (2022).

[37] A. Gourgout, A. Marguerite, B. Fauqué, and K. Behnia, Electronic thermal resistivity and quasiparticle collision cross section in semimetals, Phys. Rev. B **110**, 155119 (2024).
[38] T. Zhou and D. Gall, Resistivity scaling due to electron surface scattering in thin metal layers, Phys. Rev. B **97**, 165406 (2018).
[39] D. Gall, Electron mean free path in elemental metals, J. Appl. Phys. **119**, 085101 (2016).
[40] L. Levitov and G. Falkovich, Electron viscosity, current vortices and negative nonlocal resistance in graphene, Nat. Phys. **12**, 672 (2016).
[41] R. P. Gurzhi and S. I. Shevchenko, Hydrodynamic mechanism of electric conductivity of metals in a magnetic field, Sov. J. Exp. Theor. Phys. **27**, 1019 (1968), https://jetp.ras.ru/cgi-bin/e/index/e/27/6/p1019?a=list.
[42] Y. Huang, Q. Yu, Q. Chen, and R. Wang, Viscosity of liquid and gaseous helium-3 from 3 mK to 500 K, Cryogenics **52**, 538 (2012).
[43] S. Wang, C. Howald, and H. Meyer, Shear viscosity of liquid ^{4}He and ^{3}He-^{4}He mixtures, especially near the superfluid transition, J. Low Temp. Phys. **79**, 151 (1990).
[44] J.-P. Bonnet, L. Devesvre, and J. Artaud, and P. Moulin, Dynamic viscosity of olive oil as a function of composition and temperature: A first approach, Eur. J. Lipid Sci. Technol. **113**, 1019 (2011).
[45] M. P. Bertinat, D. S. Betts, D. F. Brewer, and G. J. Butterworth, Damping of torsional oscillations of a quartz crystal cylinder in liquid helium at low temperatures. i. viscosity of pure ^{3}He, J. Low Temp. Phys. **16**, 479 (1974).
[46] J. C. Wheatley, Experimental properties of superfluid ^{3}He, Rev. Mod. Phys. **47**, 415 (1975).
[47] G. Giuliani and G. Vignale, *Quantum Theory of the Electron Liquid*, Masters Series in Physics and Astronomy (Cambridge University Press, Cambridge, England, 2005).
[48] D. Vollhardt and P. Wolfle, *The Superfluid Phases of Helium 3* (CRC Press, Boca Raton, 1990).
[49] D. C. Tsui and R. W. Stark, de haas-van Alphen effect, magnetic breakdown, and the Fermi surface of cadmium, Phys. Rev. Lett. **16**, 19 (1966).
[50] W. R. Datars and J. R. Cook, Magnetic breakdown of open orbits in cadmium, Phys. Rev. **187**, 769 (1969).
[51] P. B. Visscher and L. M. Falicov, Galvanomagnetic properties of a single-crystal sphere by the induced-torque method. ii. magnetic breakdown in cadmium and zinc, Phys. Rev. B **2**, 1522 (1970).
[52] M. S. Steinberg, Viscosity of the electron gas in metals, Phys. Rev. **109**, 1486 (1958).
[53] A. Principi, G. Vignale, M. Carrega, and M. Polini, Bulk and shear viscosities of the two-dimensional electron liquid in a doped graphene sheet, Phys. Rev. B **93**, 125410 (2016).
[54] K. Trachenko, M. Baggioli, K. Behnia, and V. V. Brazhkin, Universal lower bounds on energy and momentum diffusion in liquids, Phys. Rev. B **103**, 014311 (2021).
[55] C. Q. Cook and A. Lucas, Electron hydrodynamics with a polygonal fermi surface, Phys. Rev. B **99**, 235148 (2019).
[56] G. Varnavides, A. Yacoby, C. Felser, and P. Narang, Charge transport and hydrodynamics in materials, Nat. Rev. Mater. **8**, 726 (2023).
[57] U. Vool, A. Hamo, G. Varnavides, Y. Wang, T. X. Zhou, N. Kumar, Y. Dovzhenko, Z. Qiu, C. A. C. Garcia, A. T. Pierce, J. Gooth, P. Anikeeva, C. Felser, P. Narang, and A. Yacoby, Imaging phonon-mediated hydrodynamic flow in WTe_2, Nat. Phys. **17**, 1216 (2021).
[58] A. Levchenko and J. Schmalian, Transport properties of strongly coupled electron–phonon liquids, Ann. Phys. (Amsterdam) **419**, 168218 (2020).

End Matter

Appendix A: Kinematic and dynamic viscosities—The kinematic viscosity is proportional to τ_{mc} and can be extracted from the experimental $\Delta\sigma$ [6,15,52,53],

$$\nu = \frac{1}{4} v_F^2 \tau_{mc}.$$

Figure 3(d) compares the extracted ν with what was reported in graphene [14]. In both cases, there is a T^{-2} dependence at low temperature. Multiplying ν by the mass density leads to dynamic viscosity, η. Figure 3(e) compares its amplitude and the temperature dependence with that of four liquids, two quantum (He isotopes) and two classical (water and olive oil). In our limited temperature range, the viscosity of electrons in Cd is larger than the universal lower bound observed in a variety of fluids [54].

Appendix B:Momentum-conserving scattering—Most charge carriers reside in the large Fermi pockets, whose large Fermi energies result in a long τ_{mr}. By contrast, the short momentum-conserving collision time emerging below 5 K is presumably associated with much smaller energy scales that have not been included in the treatment above (Table II).

TABLE II. Calculated Fermi energies of different pockets. The bottom of the electronlike pocket known as "lens" at Γ is taken as its Fermi energy. The tops of the holelike "cap" and the holelike "monster" at H define their Fermi energies. In addition, there are small energies at K point: Petty-1 is associated with the "cap" and petty-2 with the "monster." Along K–M, the lilliputian energy corresponds to a tiny local maximum [see the inset of Fig. 4(c)].

Pocket	Fermi energy (eV)
Lens	-3.05
Monster	$+1.62$
Cap	$+0.96$
Petty-1	-8.8×10^{-2}
Petty-2	-1.2×10^{-2}
Lilliputian	$+4.8 \times 10^{-4}$

Ab initio calculations incorporating spin-orbit coupling (See SM Note 4 [25]) find an intricate electronic band structure (Fig. 4) with multiple Fermi energies (Table II). Indeed, $\tau_{mc}T^2$ is roughly compatible with the lilliputian Fermi energy near the K point. Its amplitude is at the edge of the accuracy of these calculations. The existence of $\approx$1 K energy scales is also inferred by the occurrence of magnetic breakdown at very low fields [49–51] in Cd.

The Fermi surface geometry is known to play a role in the robustness of the hydrodynamic regime [55]. In cadmium, as seen in Fig. 4, the geometry is intricate. The three neighboring valleys ("monsters") almost touch at each K point of the Brillouin zone. The "monster" and the "cap" become almost degenerate near each H point. These details may play a role in widening the large gap between $\tau_{mc}T^2$ and $\tau_{mr}T^2$.

Exchange of phonons between electrons may play a role in amplifying momentum-conserving *e-e* collisions [36,56–58]. Interestingly, Cd has a large e-ph collision cross section (See SM Note 2 [25]).